ACS APPLIED MATERIALS & INTERFACES

www.acsami.org

Research Article

In Situ Embedding Synthesis of $CsPbBr_3$@Ce-MOF@SiO_2 Nanocomposites for High Efficiency Light-Emitting Diodes: Suppressing Reabsorption Losses through the Waveguiding Effect

Jiejun Ren, Andries Meijerink,* Xiaopeng Zhou, Jiapeng Wu, Gangyi Zhang, and Yuhua Wang*

Cite This: *ACS Appl. Mater. Interfaces* 2022, 14, 3176–3188

Read Online

ACCESS | Metrics & More | Article Recommendations | Supporting Information

ABSTRACT: All-inorganic perovskite quantum dots (PQDs), which possess outstanding photophysical properties, are regarded as promising materials for optoelectronic applications. However, the poor light conversion efficiency and severe stability problem hinder their widespread applications. In this work, a novel encapsulation strategy is developed through the in situ growth of $CsPbX_3$ PQDs in presynthesized mesoporous cerium-based metal organic frameworks (Ce-MOFs) and further silane hydrolysis−encapsulation, generating stable $CsPbX_3$@Ce-MOF@SiO_2 composites with greatly enhanced light conversion efficiency. Moreover, the simulation results suggest that the pore boundary of Ce-MOFs has a strong waveguide effect on the incident PQD light, constraining PQD light inside the bodies of Ce-MOFs and suppressing reabsorption losses, thus increasing the overall light conversion efficiency of PQDs. Meanwhile, the Ce-MOF@SiO_2 protective shell effectively improves the stability by blocking internally embedded PQDs from the harmful external environment. Further, the obtained white-light-emitting diode shows an ultrahigh luminous efficiency of 87.8 lm/W, which demonstrates their great potential in optoelectronic applications.

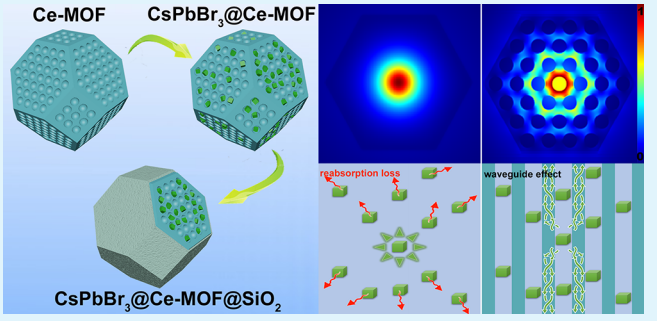

KEYWORDS: *perovskite quantum dots, mesoporous MOFs, waveguide effect, stability, LEDs*

INTRODUCTION

All-inorganic perovskite quantum dots (PQDs) have drawn enormous attention in research and practical applications owing to their excellent optical properties,[1−15] such as flexible tunability emission over the entire visible spectrum, narrow full width at half-maximum (fwhm), and ultrahigh photoluminescence quantum yield (PLQY). These advantages render their great potential in lighting and display applications, such as display backlights,[7] light-emitting diodes (LEDs),[8,9] and mini/micro-LEDs.[10] Nevertheless, the efficiency loss through reabsorption and especially the low stability are the main obstacles in realizing practical applications of PQDs in displays and LEDs.

The luminous efficiency of PQD-based white LEDs (W-LEDs) is generally low (20−60 lm/W),[4−6] which is mainly related to the low light conversion efficiency of PQDs. The overall conversion efficiency of PQDs is much lower than for traditional phosphors, which has been attributed to reabsorption losses of PQDs.[11−13] The PQDs emit light under excitation, and part of the emission is absorbed by the neighboring PQDs as the excitonic emission overlaps with the absorption. Repeated reabsorption results in an efficiency loss. Even when the quantum yield is high (e.g., 90%), the overall efficiency is reduced to 0.9^n after n reabsorption steps. The optical energy loss will also lead to an increase in operating temperature and accelerate the thermal quenching of PQDs and compromise the operational stability of the PQD-based W-LEDs. Therefore, the overall conversion efficiency becomes one of the bottlenecks in the practical application of PQD-based W-LEDs. Jeon and co-workers proposed a conversion efficiency improving strategy by coating CdSe-based QDs on the photonic crystal structure.[16] The improved interaction between the excitation photons and the CdSe-based QDs enhances the absorption of excitation photons, thereby increasing the light conversion efficiency of fabricated CdSe-based LEDs. Li et al. reported a CdSe/ZnS QD-based W-LED with high luminous efficiency by incorporating QD/SBA-15 nanoparticles onto a blue chip.[17] The improved luminous efficiency is explained by the inner scattering-induced waveguide effect of the SBA-15 matrix, which greatly reduces the reabsorption loss and increases the light conversion efficiency. However, as far as we know, the strategy to prevent the

Received: October 27, 2021
Accepted: December 16, 2021
Published: January 4, 2022

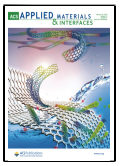

Scheme 1. Schematic Illustration of the Formation Process of $CsPbBr_3$@Ce-MOF@SiO_2 Composites

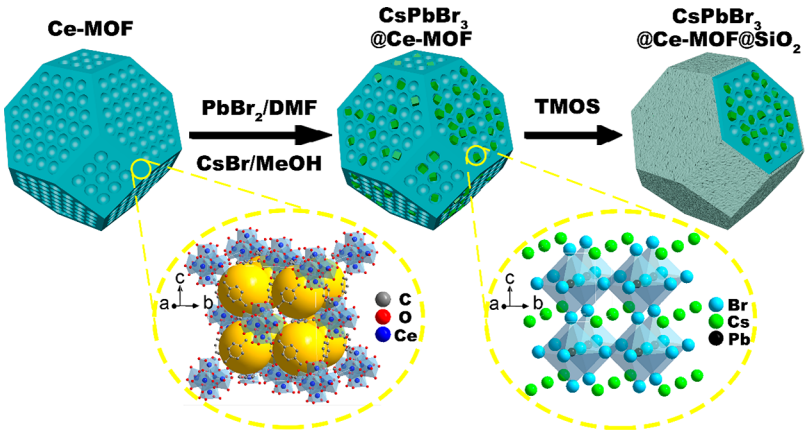

reabsorption losses and improve the light conversion efficiency of $CsPbX_3$ PQD-based LEDs through photon management by optical structures has so far not been explored.

The stability problem of $CsPbX_3$ PQDs is another challenging obstacle in the practical application of PQD W-LEDs.[18,19] Due to the ionic character and low formation energy, PQDs suffer from poor stability when exposed to high temperature, moisture, and light irradiation. Moreover, the highly dynamic binding of surface ligands could result in the aggregation and decomposition of PQDs.[20,21] In recent years, massive efforts have been devoted to improving the stability of PQDs.[22−34] Porous materials such as mesoporous silica,[35,36] mesoporous alumina,[37,38] mesoporous titania,[39] hierarchical CaF_2 nanospheres,[40] zeolitic imidazolate frameworks,[41,42] and metal−organic frameworks (MOFs)[43−50] were extensively explored to encapsulate PQDs. Among the various porous materials, MOFs with a large surface area, tunable structure and pore size, and tailorable functionalities[51−56] are an ideal matrix for encapsulating the PQDs. Li and co-workers grew $MAPbX_3$ PQDs in MOF hosts by using a Pb-MOF as the sacrificial porous template, which could be applied as a smart luminescent system toward confidential information encryption and decryption.[57] To reduce the diffusion resistance of PQDs into the pores of MOFs, we expanded the pore size of MOF-5 to the mesoporous regime via templating synthesis and embedded $CsPbX_3$ PQDs into the mesopores of MOF-5 crystals in our previous work.[58] However, the stability of PQDs needs to be further improved since the pore structures of the porous encapsulation matrix are still open to the ambient environment and expose the PQDs to external environmental factors, such as moisture and oxygen.[4,59]

Furthermore, previous research has been mainly focused on the macroscopic optical properties of PQD@MOF composites. To the best of our knowledge, there are hardly any studies paying attention to the light extraction in PQD@MOF composites from the microscopic perspective of photon management. Understanding and optimizing the internal light conversion is significant and important for improving the optical properties of PQDs. Therefore, it is critical to investigate the internal light conversion mechanism in PQD@MOF composites and design the structure of the encapsulating MOF matrix to also optimize this aspect.

Herein, we demonstrate a novel encapsulation strategy to synthesize monodispersed $CsPbX_3$@Ce-MOF@SiO_2 composites through in situ growth of $CsPbX_3$ PQDs in mesoporous Ce-MOF crystals, followed by silane hydrolysis−encapsulation. The resulting $CsPbX_3$@Ce-MOF@SiO_2 composites exhibit high PLQY with improved stability. To determine the light outcoupling of the PQD emission in $CsPbX_3$@Ce-MOF@SiO_2 composites, finite difference time-domain (FDTD) simulations were performed with different structural parameters. According to the FDTD simulation, the high overall PLQY of the $CsPbX_3$@Ce-MOF@SiO_2 composites could be attributed to the waveguiding effect of the mesoporous structure of the Ce-MOF matrix, which suppresses the self-reabsorption losses of PQDs. Moreover, the Ce-MOF@SiO_2 shell efficiently blocks the $CsPbX_3$ PQDs from the external environment, thus preventing the degradation and aggregation of $CsPbX_3$ PQDs. As a result, the $CsPbX_3$@Ce-MOF@SiO_2 composites exhibit greatly enhanced thermal stability and photostability while eliminating anion-exchange reactions, resulting in highly improved long-term stability. Furthermore, a warm white light LED with chromatic coordinates of (0.42, 0.37) and color temperature of 2924 K was achieved by depositing $CsPbX_3$@Ce-MOF@SiO_2 composites onto the lampshade of the InGaN blue chip. The fabricated remote excitation W-LEDs exhibit a top-ranked high luminous efficiency of 87.8 lm/W along with good temporal stability. In conclusion, $CsPbX_3$@Ce-MOF@SiO_2 composites were designed based on the simulation of the internal light conversion mechanism, exhibited potential for stable high-efficiency LED applications, and offered a promising double encapsulation strategy for future research on stable highly efficient PQDs.

RESULTS AND DISCUSSION

Synthesis and Characterization of $CsPbBr_3$@Ce-MOF@SiO_2 Composites. The $CsPbBr_3$@Ce-MOF@SiO_2 composites were acquired via a two-step approach, including in situ growth processes and hydrolysis−encapsulation processes, as schematically shown in Scheme 1. The Ce-MOF is a novel well-ordered meso-/microporous crystalline material, which possesses an ordered mesopore structure, large specific surface area, and good structural stability. Their diverse mesopore structures, high structural stability, and good compatibility with guest species also endow Ce-MOFs as a wonderful matrix to accommodate guests such as metal nanoparticles, nanoclusters, and luminescent materials. The mesoporous Ce-MOF was chosen as an encapsulation matrix, owing to its abundant, ordered, and uniform mesopore structure, which provides an excellent space for the confined growth of $CsPbBr_3$ PQDs. The mesoporous Ce-MOF with

https://doi.org/10.1021/acsami.1c20804
ACS Appl. Mater. Interfaces 2022, 14, 3176−3188

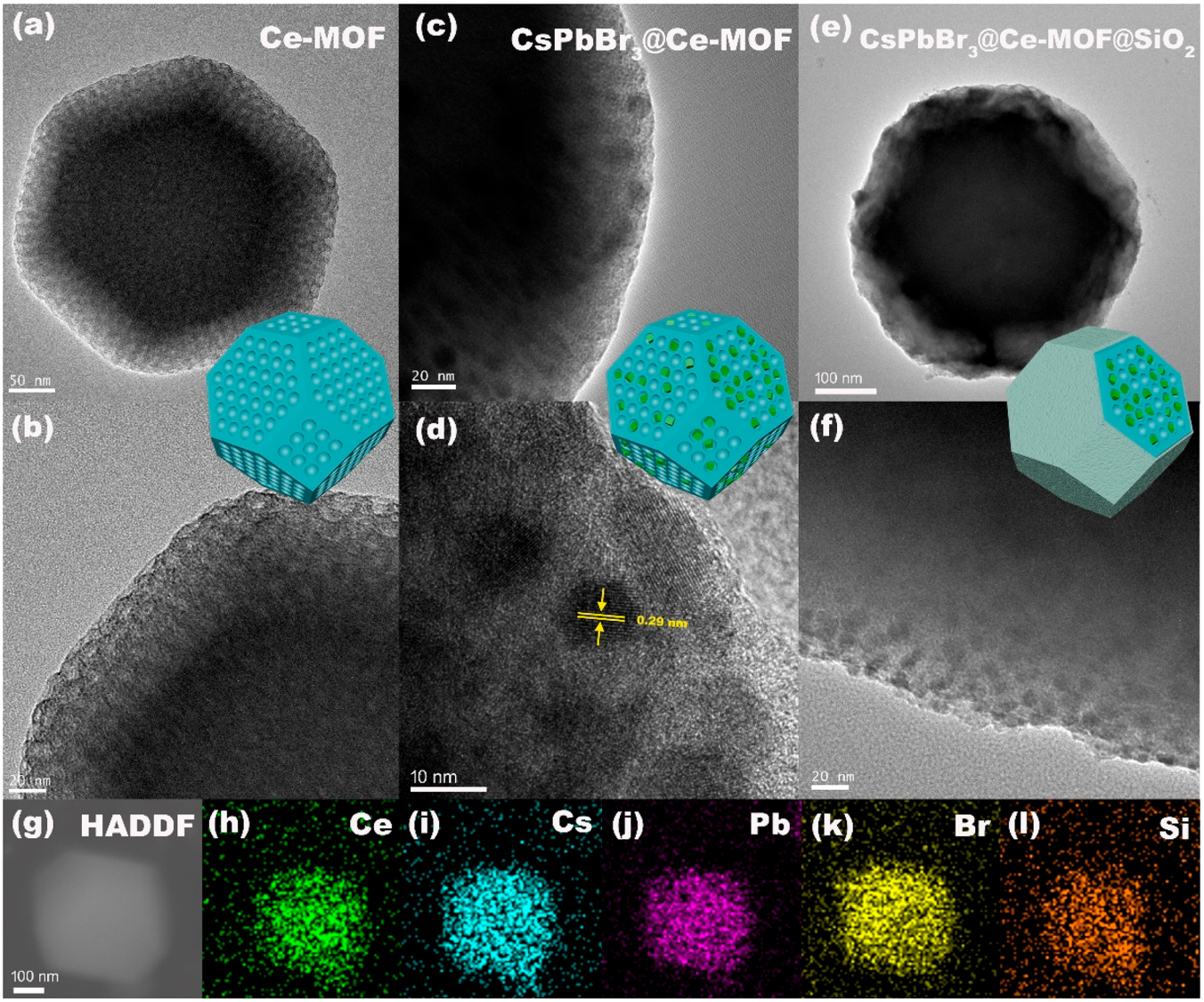

Figure 1. TEM and HR-TEM images of Ce-MOF (a, b), $CsPbBr_3$@Ce-MOF (c, d), and $CsPbBr_3$@Ce-MOF@SiO_2 (e, f). Insets: schematic illustration of the products at each stage. (g) HAADF-STEM image and STEM-EDX elemental mappings of Ce (h), Cs (i), Pb (j), Br (k), and Si (l) elements existing in $CsPbBr_3$@Ce-MOF@SiO_2 composites.

ordered mesopores and well-crystallized micropore walls was synthesized by a modified salt-mediated template strategy,[60] where Pluronic F-127 copolymers serve as soft templates, H_2BDC as a framework-building ligand, and ClO_4^- as a mediator. F-127 copolymers aggregate and form rodlike micelles, with the poly(propylene oxide) (PPO) as the core, surrounded by poly(ethylene oxide) (PEO) coronas. The PEO segments could coordinate with metal ions; therefore, the Ce-MOF could crystallize around the F-127 micelles along with the anchored Ce clusters. After the removal of the F-127 templates, the well-ordered rodlike mesopores were left in the Ce-MOF crystals. Ce nodes are attracted and bonded to the H_2BDC ligands by the Hofmeister salting-in ion ClO_4^-, which promotes the growth of the Ce-MOF as a mediator. By tailoring the ClO_4^-: Ce^{4+} feeding ratio (Figure S1), reaction temperature (Figure S2), and reaction time (Figure S3), the optimal reaction conditions for synthesizing Ce-MOFs with a well-ordered mesopore structure were obtained.

An in situ growth method was used to prepare $CsPbBr_3$@Ce-MOF composites (Stage I). First, $PbBr_2$ was impregnated into mesoporous Ce-MOF by stirring Ce-MOF crystals and $PbBr_2$ in DMF solvent under vacuum. Then, the crystals were gathered and redispersed in toluene. After that, the CsBr/MeOH solution was injected to induce the in situ growth of $CsPbBr_3$ PQDs in Ce-MOF crystals at room temperature. The hydrolysis−encapsulation process was then carried out by adding TMOS and stirring the mixture with open air (Stage II). Air moisture induces the formation of a SiO_2 coating layer around the $CsPbBr_3$@Ce-MOF by the slow hydrolysis of the terminal alkoxysilane groups of TMOS. By tailoring the hydrolysis reaction time (Figure S4), the optimal reaction conditions for coating Ce-MOFs with a uniform thin SiO_2 shell were obtained. The SiO_2 coating layer seals the open pores of $CsPbBr_3$@Ce-MOF, which impedes the leakage of $CsPbBr_3$ PQDs, modifies the surface of $CsPbBr_3$ PQDs, and protects the PQDs from the ambient atmosphere. Finally, the $CsPbBr_3$@Ce-MOF@SiO_2 composites were centrifuged and washed with toluene and then dried under vacuum. The well-ordered mesoporous Ce-MOF provides an excellent space for the growth and dispersion of the $CsPbBr_3$ PQDs, which also act as

https://doi.org/10.1021/acsami.1c20804
ACS Appl. Mater. Interfaces 2022, 14, 3176−3188

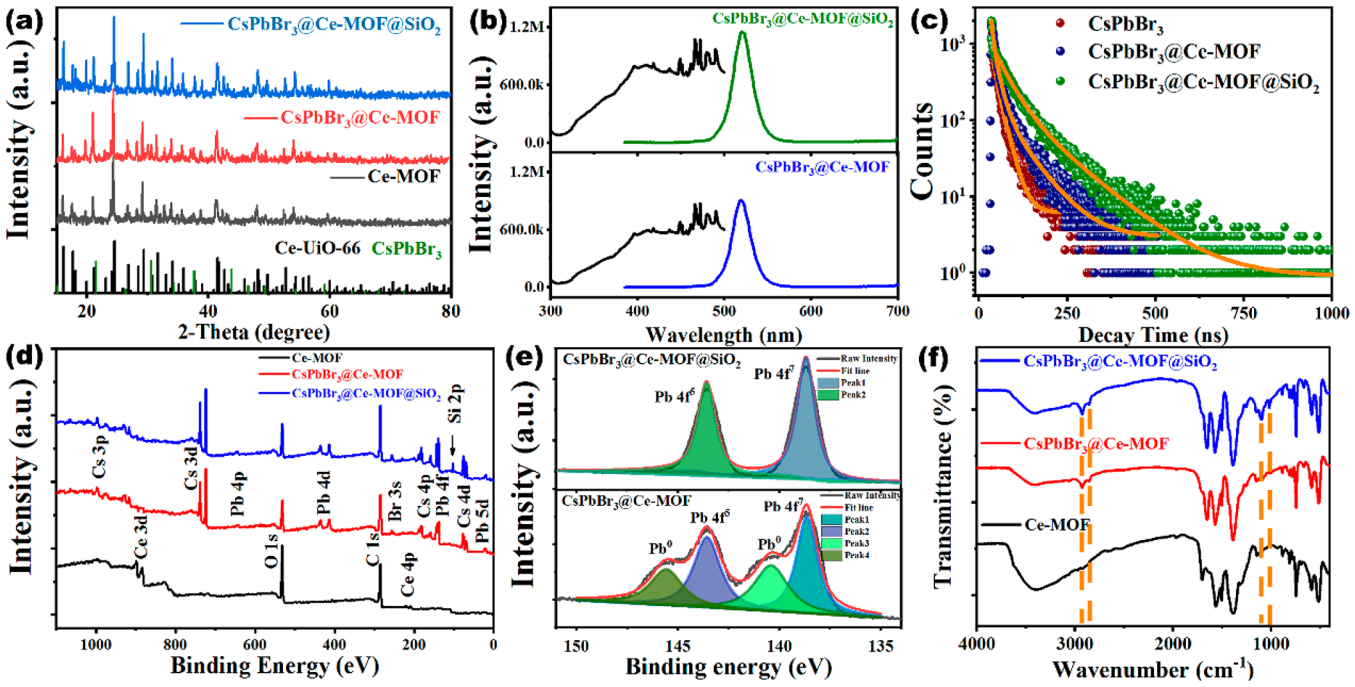

Figure 2. Characterization of Ce-MOF, $CsPbBr_3$@Ce-MOF, and $CsPbBr_3$@Ce-MOF@SiO_2 composites. (a) XRD patterns of Ce-MOF, $CsPbBr_3$@Ce-MOF, and $CsPbBr_3$@Ce-MOF@SiO_2 composites. XRD references patterns are simulated XRD patterns of the Ce-UiO-66 crystal (black line) and PDF# 54-0752 for the cubic $CsPbBr_3$ (green line). (b) PL and PLE spectra and (c) time-resolved PL decays of $CsPbBr_3$, $CsPbBr_3$@Ce-MOF, and $CsPbBr_3$@Ce-MOF@SiO_2 composites. (d) XPS spectra, (e) high-resolution XPS spectra of Pb 4f, and (f) FT-IR spectra of Ce-MOF, $CsPbBr_3$@Ce-MOF, and $CsPbBr_3$@Ce-MOF@SiO_2 composites.

a solid encapsulation matrix to provide mechanical rigidity. Moreover, the thin SiO_2 protecting shell possesses extraordinary mechanically robust and transparent properties, which can seal the open pores without affecting light transmission.

TEM and high-resolution TEM (HR-TEM) images of the products in each synthesis stage are shown in Figure 1. TEM images show that the morphology of the Ce-MOF is truncated octahedrons with a size of about 500 nm (Figure 1a). Well-ordered mesopores are found in a regular pattern arranged on the surface of the truncated octahedrons (Figure 1b). After the in situ growth of the $CsPbBr_3$ PQDs, the $CsPbBr_3$ PQDs are well embedded within the mesopores of the Ce-MOF (Figure 1c). The HR-TEM image shows an interplanar distance of 0.29 nm (Figure 1d), which corresponds to the (200) plane spacing of the cubic $CsPbBr_3$ PQDs. After the hydrolysis−encapsulation process, the composites are covered with a thin SiO_2 shell. The Ce-MOF and $CsPbBr_3$@Ce-MOF composites both possess regular and smooth surfaces. In contrast, the $CsPbBr_3$@Ce-MOF@SiO_2 composites have relatively rough surfaces with distinct wrinkles (Figure 1e), which indicate that the composites are well-covered with an amorphous silica shell. The HR-TEM image of $CsPbBr_3$@Ce-MOF@SiO_2 composites clearly shows that the open pores of the Ce-MOF are well capped, and the $CsPbBr_3$ PQDs are embedded under the SiO_2 shell (Figure 1f). The average size of the $CsPbBr_3$ PQDs in $CsPbBr_3$@Ce-MOF@SiO_2 composites is about 10.6 nm (Figure S5). The elemental mapping images of $CsPbBr_3$@Ce-MOF@SiO_2 composites are shown in Figure 1g−1l, and the Ce, Cs, Pb, Br, and Si elements are homogeneously distributed, indicating that the $CsPbBr_3$ PQDs are uniformly embedded within the Ce-MOF and that the Ce-MOF is well coated with a SiO_2 shell.

The crystal structure of the resulting $CsPbBr_3$@Ce-MOF@SiO_2 composites was identified by powder X-ray diffraction (XRD). The XRD patterns of the products at different stages of synthesis are shown in Figure 2a. The XRD pattern of the Ce-MOF matches well with the simulated pattern of pristine Ce-UiO-66 MOFs, evidencing the formation of well-crystallized pure MOF crystals. After the in situ growth of $CsPbBr_3$ PQDs and further coating with the SiO_2 shell, the XRD pattern of $CsPbBr_3$@Ce-MOF@SiO_2 nearly remains unchanged, suggesting the crystal structure of the Ce-MOF matrix is well maintained. However, the XRD pattern shows no obvious $CsPbBr_3$ peaks, which could be masked by the diffraction peaks of the Ce-MOF matrix due to the low $CsPbBr_3$ content and the small size, leading to peak broadening.

The $CsPbBr_3$@Ce-MOF@SiO_2 composites emit bright green light under UV illumination. The PL and PLE spectra of $CsPbBr_3$@Ce-MOF@SiO_2 composites are shown in Figure 2b, which shows a broad excitation spectrum spanning the UV and blue light range and a distinctive strong emission peak at 519 nm with a narrow fwhm of 24 nm. Note that the peaks around 470 nm result from intense lines from the xenon lamp used for excitation and not real features of the excitation spectrum. Comparing with $CsPbBr_3$@Ce-MOF, the PL intensity of $CsPbBr_3$@Ce-MOF@SiO_2 composites is 1.46 times higher than that of $CsPbBr_3$@Ce-MOF, which is consistent with the increase of PLQY from 56% to 78%.

In order to gain a deeper understanding of the exciton recombination dynamics in $CsPbBr_3$@Ce-MOF@SiO_2 composites, the time-resolved PL decay curves of $CsPbBr_3$ PQDs, $CsPbBr_3$@Ce-MOF, and $CsPbBr_3$@Ce-MOF@SiO_2 composites were recorded for excitation by 365 nm ultraviolet light and monitoring the 519 nm emission and are shown in Figure 2c. The time-resolved PL decay curves can be well fitted by the

https://doi.org/10.1021/acsami.1c20804
ACS Appl. Mater. Interfaces 2022, 14, 3176−3188

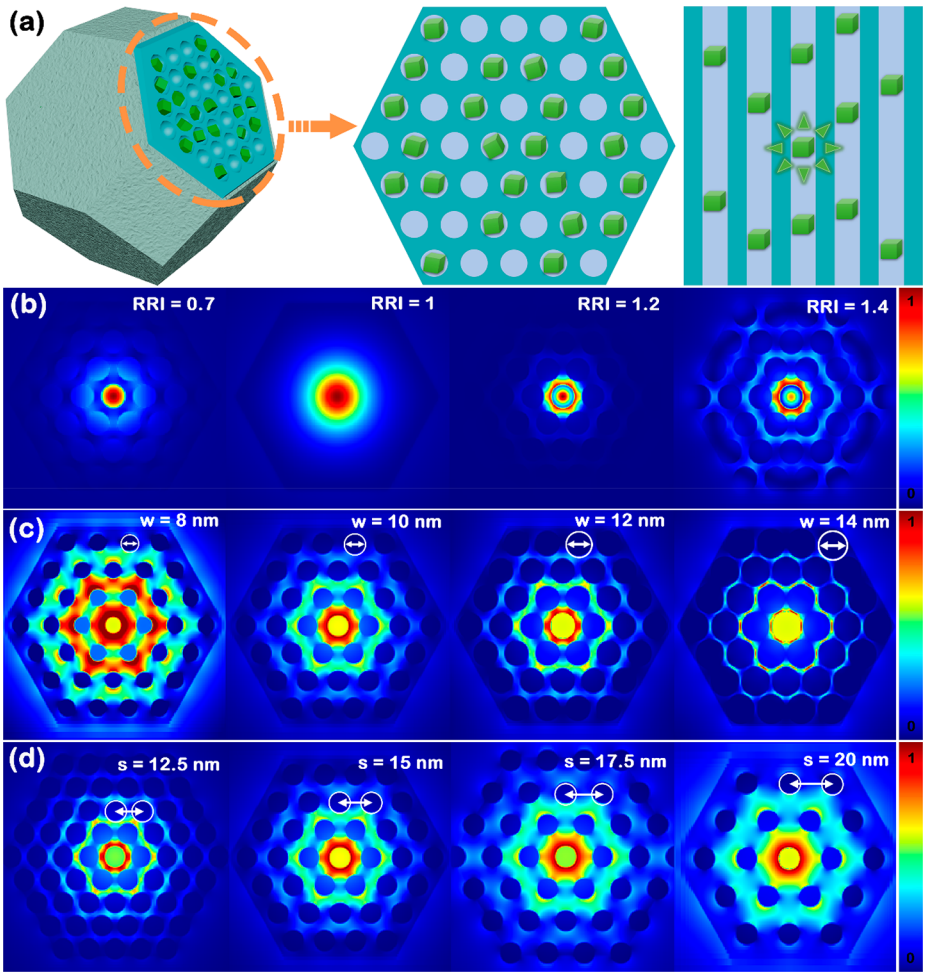

Figure 3. FDTD simulation of $CsPbBr_3$@Ce-MOF@SiO_2 composites. (a) Schematic illustration of the top view and lateral view of $CsPbBr_3$@Ce-MOF@SiO_2 in the FDTD simulation. The electric field at the top surface of $CsPbBr_3$@Ce-MOF@SiO_2 with different relative refractive index (RRI) values (b), pore width w (c), and pore spacing s (d).

biexponential function $I(t) = A_1e^{(-t/\tau_1)} + A_2e^{(-t/\tau_2)}$, and the average lifetime (τ_{ave}) can be calculated by the equation $\tau_{ave} = \frac{A_1\tau_1^2 + A_2\tau_2^2}{A_1\tau_1 + A_2\tau_2}$. The PL decay of $CsPbBr_3$@Ce-MOF@SiO_2 is well-fitted by biexponential fitting, with a short lifetime τ_1 of 6.5 ns and a long lifetime τ_2 of 61.6 ns. Furthermore, the average exciton recombination lifetime of $CsPbBr_3$@Ce-MOF@SiO_2 is 11.3 ns, which is longer than $CsPbBr_3$@Ce-MOF (9.7 ns) and $CsPbBr_3$ (7.6 ns). The longer exciton lifetimes can be explained by the ordered mesopores of Ce-MOF and the SiO_2 shell effectively passivating the surface defects of $CsPbBr_3$ PQDs and reducing the nonradiative recombination of the carriers. A reduced nonradiative recombination rate in the $CsPbBr_3$@Ce-MOF@SiO_2 composites is also consistent with the higher PLQY.

To determine the chemical compositions, the XPS spectra of Ce-MOF, $CsPbBr_3$@Ce-MOF, and $CsPbBr_3$@Ce-MOF@SiO_2 composites are shown in Figure 2d. Distinct Ce, C, and O signals could be detected in the XPS spectra of Ce-MOF (black line). With the in situ growth of $CsPbBr_3$ PQDs, strong new peaks appear in the XPS spectra of $CsPbBr_3$@Ce-MOF (red line), which could be assigned to Cs, Pb, and Br. After the growth of the SiO_2 shell, the XPS spectra of $CsPbBr_3$@Ce-MOF@SiO_2 composites contain a clear Si signal (blue line). The Pb 4f high-resolution XPS spectrum of the $CsPbBr_3$@Ce-MOF could be deconvoluted into four peaks (Figure 2e), where two main peaks located at 138.6 eV ($4f_{7/2}$) and 143.6 eV ($4f_{5/2}$) are attributed to the Pb^{2+} oxidation state and two minor peaks are assigned to metallic Pb^0. The elemental Pb nanoparticles are attached to the surface of $CsPbBr_3$ PQDs and may act as traps, leading to a decrease of the luminescence efficiency.[61] After SiO_2 coating, the additional two weaker peaks are absent, which indicates that the SiO_2 coating prevents the formation of Pb nanoparticles on the $CsPbBr_3$ PQDs and modifies the surface of the $CsPbBr_3$ PQDs. These results correspond well to the PLQY increase after SiO_2 coating.

In order to further confirm the in situ growth of $CsPbBr_3$ PQDs and the silica coating process, Fourier transform infrared (FTIR) spectra of Ce-MOF, $CsPbBr_3$@Ce-MOF, and $CsPbBr_3$@Ce-MOF@SiO_2 composites were measured and analyzed, which are shown in Figure 2f. The absorption bands of carboxylate groups, skeletal vibrations, and bending vibrations of the benzene ring (1573, 1518−1390, and 748−514 cm^{-1}) could be clearly observed in the FTIR spectra of Ce-MOF, $CsPbBr_3$@Ce-MOF, and $CsPbBr_3$@Ce-MOF@SiO_2. After the in situ growth of $CsPbBr_3$ PQDs, two new absorption bands emerged at 2927 and 2854 cm^{-1}. These two new adsorption bands could be assigned to the C−H asymmetric and symmetric stretching vibrations and are

https://doi.org/10.1021/acsami.1c20804
ACS Appl. Mater. Interfaces 2022, 14, 3176−3188

attributed to the ligands of $CsPbBr_3$ PQDs.[59] The formation of the SiO_2 shell can be verified by sharp peaks around 1100 and 1020 cm^{-1} in the FTIR spectrum of $CsPbBr_3$@Ce-MOF@SiO_2, which can be ascribed to stretching vibrations of Si−O bonds.

Furthermore, Brunauer−Emmett−Teller (BET) N_2 adsorption−desorption isotherms were measured and analyzed to explore the porous nature of Ce-MOF, $CsPbBr_3$@Ce-MOF, and $CsPbBr_3$@Ce-MOF@SiO_2 composites. The N_2 adsorption−desorption isotherm of the Ce-MOF (black line in Figure S6a) shows a combination of a Type-I and Type-IV isotherms with a large H2-type hysteresis loop (delayed capillary evaporation step), implying the simultaneous existence of micropores and uniform cage-type mesopores with a small entrance in the Ce-MOF.[62] Using the Barrett−Joyner−Halenda method, the distribution of pore diameters is calculated and shown in Figure S6b. The pore diameter of the Ce-MOF is determined to be about 12.6 nm; the total BET surface area is around 1064 m^2/g; and the total pore volume is around 0.68 cm^3/g (Table S1). After the in situ growth of $CsPbBr_3$ PQDs, the pore volume of $CsPbBr_3$@Ce-MOF significantly decreased to 0.37 cm^3/g, which could be ascribed to the mesopores of Ce-MOF being filled by nonporous $CsPbBr_3$ PQDs. The sharply decreased pore volume also represents the high loading rate of the PQDs in the pores of Ce-MOF. After SiO_2 coating, the $CsPbBr_3$@Ce-MOF@SiO_2 composites exhibit a dramatically decreased pore volume and surface area which indicate that the open pores are well sealed.

Light Propagation in $CsPbBr_3$@Ce-MOF@SiO_2 Composites. To investigate the effect of mesopore arrays in the Ce-MOF matrix on the light propagation of $CsPbBr_3$ PQDs, a three-dimensional FDTD simulation was performed. The classical optical reflection law (Snell's law) is no longer applicable when the wavelength is on the same order of magnitude as the characteristic size of the object. Thus, FDTD simulation is necessary to investigate the light propagation in nano systems.

Based on structural characteristics of Ce-MOF, a simplified truncated octahedral model with uniformly distributed inwardly extending pores was used to study the light propagation mechanism in $CsPbBr_3$@Ce-MOF@SiO_2 composites. We chose the cross section of the Ce-MOF truncated octahedron as the research object, and established a simplified model in the FDTD simulation (Figure S7). The top and lateral views of $CsPbBr_3$@Ce-MOF@SiO_2 composites in the FDTD simulation are shown in the schematic diagram in Figure 3a. In the simulation, the Maxwell's curl equations are solved by using the FDTD method. Three dipole sources with wave vectors along the *x*, *y*, and *z* axes are set in the center of the model, which is regarded as the point source of PQDs.[63] The boundary condition of the calculation region is set as a perfectly matched layer (PML) to absorb the escaped lights. To record the electromagnetic energy distributions of propagating light, electromagnetic field detectors are set at the top surface of the model.

The relative refractive index (RRI) is defined as the ratio of the refractive index of Ce-MOF to that of silicone. The results of the FDTD simulation with different RRIs are shown in Figure 3b, and the distribution of electric field represents the distribution of the PQD light energy. (1) When the RRI < 1, the electric field diagram shows the pattern of the mesopore array in which the PQD emission tends to be confined in the pores of Ce-MOF. The mesopore array serves as the waveguide structure for PQD emission, inhibiting its propagation in the Ce-MOF body. Since there are many PQDs in the hole array, the restraint of the PQD light in the nanopore array will cause more reabsorption losses and thus reduces the light conversion efficiency.[17] (2) When the RRI = 1, the optical energy diverges evenly around due to the isotropic emission property of PQD emission. (3) When the RRI > 1, the electric field diagram shows the pattern of the Ce-MOF matrix, which shows that the PQD emission is mainly restrained in the Ce-MOF bodies. Due to the internal scattering effect of the ordered pore structure of Ce-MOFs, the propagation of the PQD emission is interfered with when incident with the pore boundary of the Ce-MOF matrix. The Ce-MOF matrix possesses a unique ordered structure and internal scattering effect, which provide it with a strong waveguiding effect and constrain PQD light in Ce-MOF bodies. Through this waveguide effect, the emission bypasses the neighboring PQDs located in the pore array,[17] which reduces the probability of PQD light being captured by neighboring PQDs, thus reducing self-reabsorption losses and increasing the light extraction efficiency (Figure S8). As the RRI increases further, this phenomenon becomes more apparent, and a stronger waveguide effect could be observed.

To better understand the waveguide effect of PQD emission in the Ce-MOF, the effect of the structural parameters (pore width *w*, pore spacing *s*) of the Ce-MOF nanopore structure is further explored. The FDTD simulation results for different pore widths (the RRI is kept at 1.4, and the pore space is kept at 15 nm) are shown in Figure 3c. When the pore width is 8 nm, a strong waveguide effect can be clearly observed. The optical energy of PQD emission decreases as pore width increases. When the pore width increases, the waveguide effect becomes weaker, constraining less light in Ce-MOF bodies. The reason is that a larger pore width results in a smaller characteristic size of the structure, which makes the difference between the characteristic structure and the wavelength of the PQD emission even larger, thus weakening the waveguide effect. The FDTD simulation results with different pore spacing (the RRI is kept at 1.4, and pore width is kept at 10 nm) are shown in Figure 3d. The waveguide effect becomes more and more pronounced as the pore spacing increases from 12.5 to 20 nm. This could be because the increased pore spacing of the Ce-MOF represents a more comparable characteristic size to the wavelength of the incident light, which strengthens the waveguide effect.[17]

In summary, from the perspective of reduced light reabsorption and improving light conversion efficiency, a higher refractive index, a smaller pore width, and a larger pore spacing are desired for the matrix for encapsulating PQDs. However, from the perspective of in situ growth of PQDs, a matrix with large pore width (>10 nm) is preferred. Therefore, although smaller pore width is desired for decreasing light reabsorption, a matrix with a pore width less than 10 nm is not preferred. The Ce-MOF crystals possess relatively small pore width (∼10 nm) and large pore spacing (∼18 nm), thus strengthening the waveguide effect, which renders it an excellent matrix for encapsulating PQDs (Figure S9).

Stability Tests of $CsPbBr_3$@Ce-MOF@SiO_2 Composites. It is known that $CsPbX_3$ PQDs suffer from severe stability problems, which hinders the application of $CsPbX_3$ PQDs. To demonstrate the improved stability and potential of $CsPbX_3$@Ce-MOF@SiO_2 composites in practical applications, the stabilities of $CsPbBr_3$@Ce-MOF@SiO_2 composites against

https://doi.org/10.1021/acsami.1c20804
ACS Appl. Mater. Interfaces 2022, 14, 3176−3188

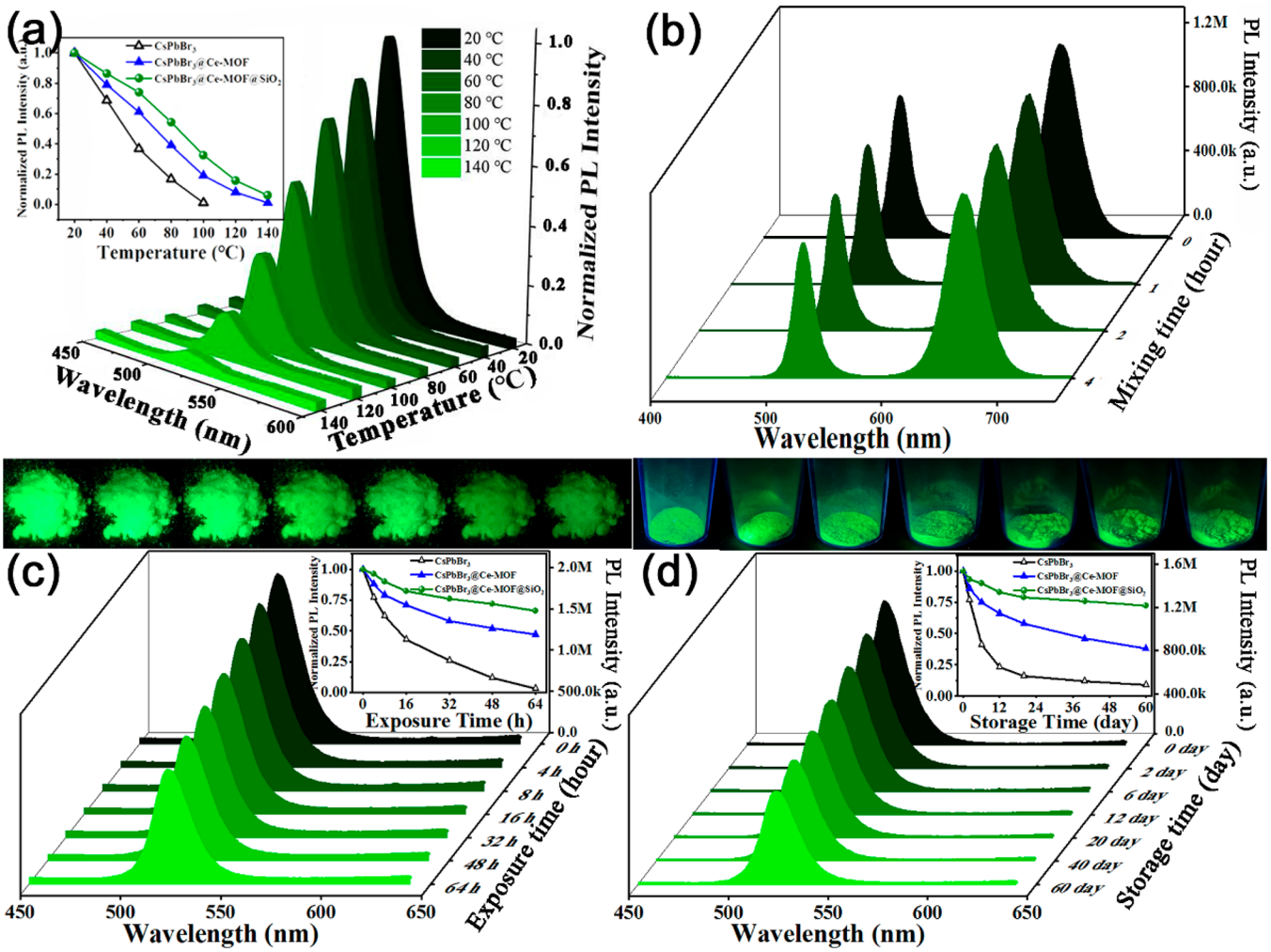

Figure 4. Stability tests of $CsPbBr_3$@Ce-MOF@SiO_2 composites. (a) Thermal stability test of $CsPbBr_3$@Ce-MOF@SiO_2 composites. Insets: temperature-dependent normalized PL intensity of $CsPbBr_3$ PQDs (black line), $CsPbBr_3$@Ce-MOF (blue line), and $CsPbBr_3$@Ce-MOF@SiO_2 (green line) composites. (b) Anion exchange resistance test between $CsPbBr_3$@Ce-MOF@SiO_2 and $CsPbBrI_2$@Ce-MOF@SiO_2 composites. (c) Photostability test of $CsPbBr_3$@Ce-MOF@SiO_2 composites. Insets: illumination time-dependent normalized PL intensity of $CsPbBr_3$ PQDs (black line), $CsPbBr_3$@Ce-MOF (blue line), and $CsPbBr_3$@Ce-MOF@SiO_2 (green line) composites. (d) Long-term storage stability test of $CsPbBr_3$@Ce-MOF@SiO_2 composites. Insets: storage time-dependent normalized PL intensity of $CsPbBr_3$ PQDs (black line), $CsPbBr_3$@Ce-MOF (blue line), and $CsPbBr_3$@Ce-MOF@SiO_2 (green line) composites.

thermal degradation, anion exchange, photobleaching, and ambient atmosphere were investigated. The thermal stability tests of $CsPbBr_3$@Ce-MOF@SiO_2 composites are shown in Figure 4a. The PL intensity of $CsPbBr_3$@Ce-MOF@SiO_2 composites gradually decreased with elevated temperature, while the PL peak position remained nearly unchanged. Upon heating, bare $CsPbBr_3$ PQDs suffered from drastic losses in PL intensity and were totally quenched at 80 °C (inset of Figure 4a). In contrast, the $CsPbBr_3$@Ce-MOF@SiO_2 composites exhibited much better thermal stability, which preserve 54% of its original PL intensity at 80 °C and keep emitting even when heated to 140 °C. After high-temperature heating, the bare $CsPbBr_3$ PQDs show the formation of an impurity phase, which could be due to the formation of high energy gap phase Cs_4PbBr_6 (Figure S10). The XRD pattern of the $CsPbBr_3$@Ce-MOF@SiO_2 composite is unchanged after heating, and the TEM image of the $CsPbBr_3$@Ce-MOF@SiO_2 composite also shows that there is only cubic $CsPbBr_3$ with no other phase (Figure S11), indicating that the encapsulation prevents phase transformation. The Ce-MOF@SiO_2 protecting shells are good insulators, which can effectively isolate the PQDs and prevent heat propagation between the heater source and PQDs.[18] Also, PQDs are well dispersed in the mesopores of the Ce-MOF matrix, which can suppress the heating-induced aggregation and reduce the thermal damage effectively.[19]

A fast anion-exchange reaction takes place in mixtures of $CsPbX_3$ PQDs, which is an undesirable effect for their application.[64] The flexible component and emission of the mixed $CsPbX_3$ PQDs also indicate the instability of bare $CsPbX_3$ PQDs. As demonstrated in Figure 4b, there is no spectral shift 4 h after mixing of green-emitting $CsPbBr_3$@Ce-MOF@SiO_2 composites and red-emitting $CsPbBrI_2$@Ce-MOF@SiO_2 composites. The Ce-MOF matrix and SiO_2 shell effectively block the anion exchange, which eliminates the obstacle to its application in light-emitting devices where the color change as a result of anion exchange is unacceptable.

The photostability is also a great challenge for $CsPbX_3$ PQDs. Under the illumination with a high intensity of UV or blue light, the $CsPbX_3$ PQDs suffer from severe fluorescence quenching, which could be due to light-induced aggregation

https://doi.org/10.1021/acsami.1c20804
ACS Appl. Mater. Interfaces 2022, 14, 3176−3188

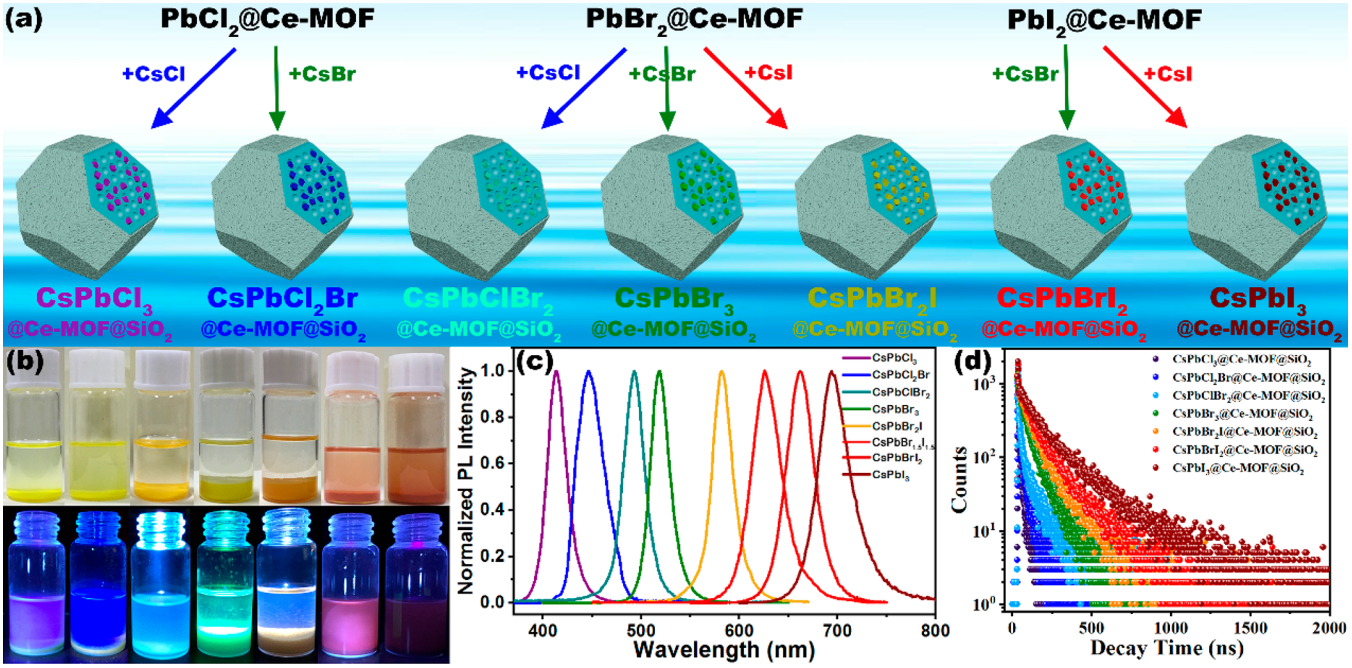

Figure 5. (a) Schematic illustration of the preparation of the $CsPbX_3$@Ce-MOF@SiO_2 composites. (b) Photographs of the $CsPbX_3$@Ce-MOF@SiO_2 composites stored in toluene under sunlight (top) and under UV light (bottom). (c) Normalized PL spectra and (d) time-resolved PL decay curves of the $CsPbX_3$@Ce-MOF@SiO_2 composites.

and/or surface reactions. To investigate the photostability, bare $CsPbBr_3$ PQDs, $CsPbBr_3$@Ce-MOF, and $CsPbBr_3$@Ce-MOF@SiO_2 composites were exposed to an ultraviolet lamp (λ = 365 nm, 0.192 W/cm^2). The photostability test results and corresponding photographs are shown in Figure 4c. The $CsPbBr_3$@Ce-MOF@SiO_2 composites preserve 65% of their original PL intensity under UV light illumination after 64 h, while the PL of bare $CsPbBr_3$ PQDs almost vanished (3.4%). Effective Ce-MOF@SiO_2 encapsulation can maintain the bonding ligands on the surface of PQDs and avoid the formation of surface traps, preventing photoinduced ligand desorption and the regrowth of the crystal.[19]

Moreover, the $CsPbBr_3$ PQD solids suffer from long-term storage stability problems, as the PQDs easily degrade under the combined action of oxygen and moisture in the ambient environment. To test the long-term storage stability, bare $CsPbBr_3$ PQDs, $CsPbBr_3$@Ce-MOF, and $CsPbBr_3$@Ce-MOF@SiO_2 composites were stored in ambient air at room temperature, and the PL spectra were measured at regular time intervals. As shown in Figure 4d, $CsPbBr_3$@Ce-MOF@SiO_2 composites preserve 76% PL intensity after being stored for 60 days and keep emitting even after six months, while the $CsPbBr_3$ PQD solids lost almost all brightness after 20 days of storage.

Comparing with other reported encapsulation strategies, the stability improvement of $CsPbX_3$ PQDs in this work is superior (Table S2). Although the testing conditions and PQD composition in Table S2 are not always the same and not all stability tests are reported for all materials, it is evident that the stability of our $CsPbBr_3$@Ce-MOF@SiO_2 composites compares favorably with the encapsulation methods. The degradation of the $CsPbX_3$ PQDs has been found to be related to unstable surface ligands and subsequent particle aggregation. In the case of $CsPbBr_3$@Ce-MOF@SiO_2 composites, the Ce-MOF matrix and the SiO_2 shell layer work synergistically to protect the $CsPbBr_3$ PQD core from ligand detachment and surface reactions. On one hand, the uniformly distributed mesopores of the Ce-MOF matrix avoid the direct contact between $CsPbBr_3$ PQDs, thus preventing the aggregation of the $CsPbBr_3$ PQDs. On the other hand, the SiO_2 shell layer acts as a protective shell for the $CsPbBr_3$ PQD core, which blocks the $CsPbBr_3$ PQDs from the harmful external environment.

Synthesis and Characterization of Full-Spectrum $CsPbX_3$@Ce-MOF@SiO_2 Composites. The $CsPbX_3$@Ce-MOF@SiO_2 composites allow for flexible tuning of the band gap via modulating the anion composition through the ratio of Cl/Br/I of the precursors. As a result, the emission color can be tuned continuously over the entire visible spectrum. To investigate the universality and potential applications of the $CsPbX_3$@Ce-MOF@SiO_2 composites, we prepared composites with different emission colors. As the schematic illustration in Figure 5a shows, a series of $CsPbX_3$@Ce-MOF@SiO_2 composites were synthesized by changing the composition through the precursors. Photographs of the $CsPbX_3$@Ce-MOF@SiO_2 composites stored in toluene under sunlight and UV light are shown in Figure 5b. The $CsPbX_3$@Ce-MOF@SiO_2 composites settle at the bottom of toluene solution and emit colorful light under UV excitation, while the supernatant remains nonemissive. These results prove that the SiO_2 shell completely seals the open pores of the Ce-MOF matrix and prevents the leakage of the $CsPbX_3$ PQDs. The PLQYs of $CsPbX_3$@Ce-MOF@SiO_2 composites are listed in Table S3. The $CsPbBr_3$@Ce-MOF@SiO_2 composite shows the highest PLQY among the $CsPbX_3$@Ce-MOF@SiO_2 composites. The PL spectra of $CsPbX_3$@Ce-MOF@SiO_2 composites are shown in Figure 5c, which exhibit distinctive narrow emission peaks and cover the entire visible spectral region from violet (410 nm) to dark red (695 nm). With the substitution of Cl by Br and I, the emission peaks gradually red shift to a longer wavelength, which is well-known and ascribed to the decreasing band gap energies of the

https://doi.org/10.1021/acsami.1c20804
ACS Appl. Mater. Interfaces 2022, 14, 3176−3188

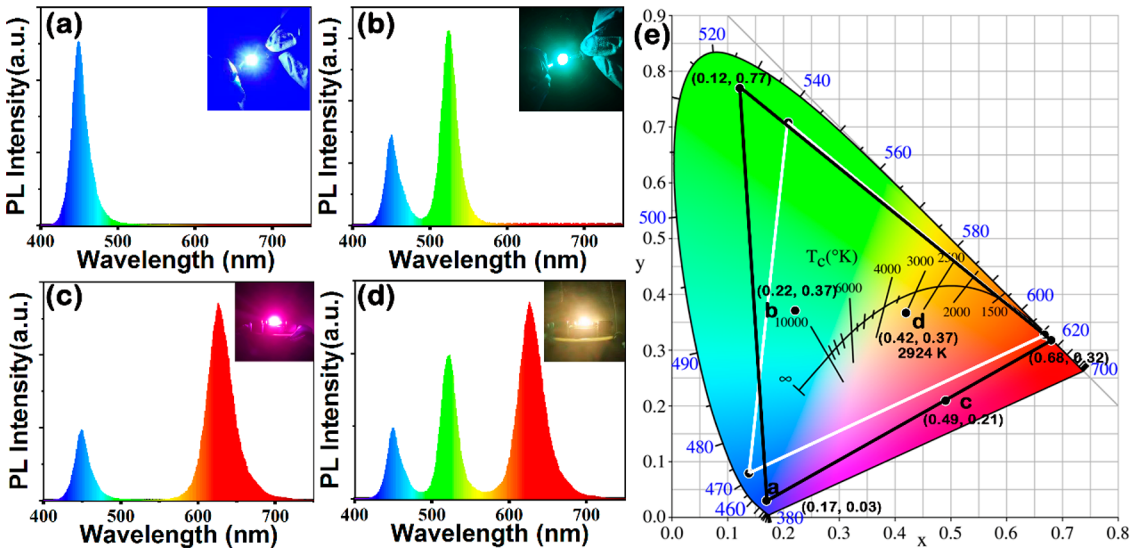

Figure 6. Emission spectra and corresponding photographs of (a) blue InGaN LED, (b) green $CsPbBr_3$@Ce-MOF@SiO_2 LED, (c) red $CsPbBr_{1.5}I_{1.5}$@Ce-MOF@SiO_2 LED, and (d) white $CsPbX_3$@Ce-MOF@SiO_2 LED at a driving current of 10 mA. (e) CIE color coordinates of the blue chip, green $CsPbBr_3$@Ce-MOF@SiO_2 composites, red $CsPbBr_{1.5}I_{1.5}$@Ce-MOF@SiO_2 composites, and the fabricated LEDs.

$CsPbX_3$ PQDs. The broadness of the emission peaks of I containing $CsPbX_3$@Ce-MOF@SiO_2 composites is ascribed to less-ordered arrangements of the halides in the lattices, which could be due to the difference between Br and I ionic radii. The CIE color coordinates of $CsPbX_3$@Ce-MOF@SiO_2 composites are shown in Figure S12. Note that the fwhm of the red light (35 nm) is higher than the fwhm of the green light (23 nm); yet, the color purity of the green light is about 86%, while the color purity of the red light is close to 100%. The relation between the width of emission bands and color purity varies for different emission wavelengths, as outlined in the seminal work by MacAdam on color perception.[65] The time-resolved PL curves of $CsPbX_3$@Ce-MOF@SiO_2 composites are shown in Figure 5d and could be fitted by a dual-exponential function. The average lifetime is longer for the heavier halides (I > Br > Cl), ranging from 33 ns ($CsPbI_3$@Ce-MOF@SiO_2) to 5 ns ($CsPbCl_3$@Ce-MOF@SiO_2), which is consistent with previous reports.[1]

Preparation and Characterization of $CsPbX_3$@Ce-MOF@SiO_2-Based LEDs. As discussed above, the $CsPbX_3$@Ce-MOF@SiO_2 composites possess excellent PL properties with improved stability, rendering them promising in optoelectronic applications. To further explore the potential application in LEDs, the $CsPbX_3$@Ce-MOF@SiO_2 composites were deposited onto a blue LED chip to fabricate PQD-LEDs of different colors. Due to the fast anion exchange reaction between different $CsPbX_3$ PQDs, $CsPbX_3$ W-LEDs are generally fabricated by the combination of $CsPbX_3$ PQDs with commercial phosphors or by constructing a multilayer $CsPbX_3$ PQD structure to avoid direct contact between $CsPbX_3$ PQDs of different anion composition. Because of the Ce-MOF@SiO_2 protecting shell, the $CsPbX_3$@Ce-MOF@SiO_2 composites exhibit improved stability and good anion exchange resistance, which allow for mixing different PQDs in a single color conversion layer of W-LEDs. Therefore, the $CsPbX_3$@Ce-MOF@SiO_2 composites were blended with ultraviolet curing adhesive to form a single down-conversion layer in this work. The mixture was deposited onto the lampshade of a blue-emitting InGaN LED chip to avoid the residual heat of a blue LED chip. After curing under ultraviolet light for 5 min, a $CsPbX_3$@Ce-MOF@SiO_2-based LED was obtained.

The emission spectra and photographs of the blue InGaN chip (Figure 6a), LED with green $CsPbBr_3$@Ce-MOF@SiO_2 (Figure 6b), and LED with red $CsPbBr_{1.5}I_{1.5}$@Ce-MOF@SiO_2 (Figure 6c) shown for a driving current of 10 mA are shown in Figure 6. The PL maximum matched well with the PL peaks of the corresponding $CsPbX_3$@Ce-MOF@SiO_2 composites, which indicates that the LED packaging process did not affect the PL properties of the $CsPbX_3$@Ce-MOF@SiO_2 composites. By modifying the feeding ratio of the green $CsPbBr_3$@Ce-MOF@SiO_2 and the red $CsPbBr_{1.5}I_{1.5}$@Ce-MOF@SiO_2, a white light $CsPbX_3$@Ce-MOF@SiO_2 LED could be obtained (shown in Figure 6d). The $CsPbX_3$@Ce-MOF@SiO_2 W-LED emits warm white light under the operating current of 10 mA, with CIE chromaticity color coordinates of (0.42, 0.37) and a correlated color temperature (CCT) of 2924 K (Figure 6e). The CIE chromaticity color coordinates of the blue chip, green $CsPbBr_3$@Ce-MOF@SiO_2 composites, and red $CsPbBr_{1.5}I_{1.5}$@Ce-MOF@SiO_2 composites are located at (0.17, 0.03), (0.12, 0.77), and (0.68, 0.32), which encompassed 125% of the National Television System Committee (NTSC) standard which is very favorable for display applications. The $CsPbX_3$@Ce-MOF@SiO_2 W-LED exhibits a color-rendering index value of 84 and a high luminous efficiency of 87.8 lm/W, which illustrates the excellent luminous performance of $CsPbX_3$@Ce-MOF@SiO_2 W-LEDs. Upon increasing the working current, the electroluminescence (EL) intensity was gradually enhanced with no spectral shift (Figure S13). The luminous efficiency reaches maximal values of 87.8 lm/W at 10 mA and decreases upon further increasing of the working current. The high efficiency of the $CsPbX_3$@Ce-MOF@SiO_2 W-LED is outstanding and higher than previously reported results for PQD-based W-LEDs (Table S4). Meanwhile, the luminous intensity of the $CsPbX_3$@Ce-MOF@SiO_2 W-LED has no obvious variation after several hours of continuous operation, while the intensity of the green light and red light of bare $CsPbX_3$ PQD-base W-LEDs dramatically decreased with prolonged operating time (Figure S14). The long duration tests show the great promise of the $CsPbX_3$@Ce-MOF@SiO_2 in LED applications.

https://doi.org/10.1021/acsami.1c20804
ACS Appl. Mater. Interfaces 2022, 14, 3176−3188

All these results imply that $CsPbX_3$@Ce-MOF@SiO_2 composites have good prospects for various optoelectronic applications.

CONCLUSION

In summary, we reported a novel two-step encapsulation strategy with the in situ growth of $CsPbX_3$ PQDs in mesoporous Ce-MOF and further silane hydrolysis sealing. The resulting $CsPbX_3$@Ce-MOF@SiO_2 composites have a high PLQY and significantly improved stability. The $CsPbX_3$ PQDs are confined in the mesopores of the Ce-MOF, which ensures size control with a narrow size distribution. The light outcoupling was modeled by FDTD simulations which reveal that the pore boundary of the Ce-MOF matrix has a waveguide effect on the incident PQD emission, thereby reducing the self-reabsorption losses. The structural parameter of the synthesized Ce-MOF matches well with requirements for strong waveguide effects (high refractive index, small pore width, and large pore spacing), which are beneficial for reducing the self-reabsorption loss. Moreover, the Ce-MOF@SiO_2 protecting shell protects the $CsPbX_3$ PQDs from the harmful external environment, giving the PQDs highly improved stability (thermal stability, photostability, long-term storage stability, and anion exchange resistance). A W-LED was fabricated with green- and red-emitting $CsPbX_3$@Ce-MOF@SiO_2 and was shown to exhibit a top-ranked high luminous efficacy of 87.8 lm/W at 10 mA. The high stability and efficient PL of the $CsPbX_3$@Ce-MOF@SiO_2 composites reported here show great potential in light-emitting devices. Yet, the exploration of its application is still limited. Enormous efforts are still needed to further explore and realize commercial application in LEDs, displays, and micro-LEDs. This work demonstrates a novel encapsulation strategy to accelerate the commercial applications of $CsPbX_3$ PQDs and may inspire the development of other double encapsulation strategies to further improve the performance of PQDs in optoelectronic applications.

METHODS

Materials and Chemicals. Cerium(IV) ammonium nitrate ($(NH_4)_2Ce(NO_3)_6$, 99.9%, Aldrich), 1,4-dicarboxybenzene (H_2BDC, 98%, Aldrich), Pluronic F-127 ($PEO_{106}PPO_{70}PEO_{106}$, Aldrich), sodium perchlorate monohydrate ($NaClO_4{\cdot}H_2O$, 99.9%, Aldrich), acetic acid (HAc, 99.8%, Aladdin), *N*,*N*-dimethylformamide (DMF, 99%, Aladdin), ethanol (CH_3CH_2OH, 99.8%, Aladdin), cesium chloride (CsCl, 99.9%, Aldrich), cesium bromide (CsBr, 99.9%, Aldrich), cesium iodide (CsI, 99.9%, Aldrich), lead chloride ($PbCl_2$, 99.8%, Aladdin), lead bromide ($PbBr_2$, 99.8%, Aladdin), lead iodide (PbI_2, 99.8%, Aldrich), oleic acid (OA, 98%, Aldrich), oleylamine (OAm, 98%, Aldrich), methyl alcohol (MeOH, 99.8%, Aladdin), tetramethoxysilane (TMOS, 98%, Aladdin), and toluene ($C_6H_5CH_3$, 99.8%, Aladdin) were used as starting reagents without any further purification.

Synthesis of Ce-MOFs. The Ce-MOF was synthesized according to a reported method with slight modifications.[60] Pluronic F-127 (0.504 g, 0.04 mmol), $NaClO_4{\cdot}H_2O$ (2.247 g, 16 mmol), and HAc (1.2 mL, 21 mmol) were dissolved in 24 mL of deionized water. The mixture was stirred at 50 °C until the complete dissolution of Pluronic F-127. Then, $(NH_4)_2Ce(NO_3)_6$ (2.194 g, 4 mmol) and H_2BDC (0.665 g, 4 mmol) were added and stirred for 20 min at 70 °C. The resultant solids were purified through centrifugation at 8000 rpm and washed with water until the pH of the supernatant became neutral. Then, the precipitates were soaked in ethanol overnight at 50 °C to remove the remaining templates. Finally, the as-synthesized Ce-MOF crystals were obtained after being dried at 50 °C under vacuum.

Synthesis of $CsPbX_3$@Ce-MOF (X = Cl, Br, or I). Typically, 5 mmol of PbX_2 (X = Cl, Br, or I), 50 μL of OA, 50 μL of OAm, and 10 mL of DMF (DMSO for $PbCl_2$) were placed in a 20 mL glass vial and stirred at 80 °C to form a homogeneous solution. After completing dissolution of the PbX_2 salt, the as-prepared Ce-MOF (0.2 g) and PbX_2 solution were mixed and stirred under vacuum for 6 h at room temperature. The powder was collected by centrifugation under 8000 rpm for 3 min and redispersed in toluene (10 mL). In a separate solution, CsX (1 mmol) was dissolved in MeOH (10 mL) at 60 °C. Then, the CsX/MeOH solution was injected into the PbX_2/toluene precursor solution at room temperature and reacted for 2 min to form the $CsPbX_3$@Ce-MOF composites.

Synthesis of $CsPbX_3$@Ce-MOF@SiO_2 (X = Cl, Br, or I). In a typical synthesis of the silica encapsulation shell, 0.5 mL of TMOS was added to the above $CsPbX_3$@Ce-MOF/toluene solution at ambient atmosphere with continuous stirring. After a hydrolysis reaction for 4 h, the precipitates were collected by centrifuging at 8000 rpm for 3 min. Finally, the $CsPbX_3$@Ce-MOF@SiO_2 composites were obtained after being dried at 50 °C under vacuum.

Fabrication of $CsPbX_3$@Ce-MOF@SiO_2-Based LEDs. To fabricate $CsPbX_3$@Ce-MOF@SiO_2-based LEDs, $CsPbX_3$@Ce-MOF@SiO_2 composites were dispersed in an ultraviolet (UV) curing adhesive (Ergo optical adhesive 8500) and stirred evenly. Next, the mixture was deposited onto the lampshade of an InGaN blue chip (λ_{max} = 450 nm) to form a remote excitation LED structure. After curing under UV light for 5 min, the mixture was completely solidified, and the $CsPbX_3$@Ce-MOF@SiO_2-based LEDs were obtained.

Characterization. The transmission electron microscopy (TEM) and scanning transmission electron microscopy (STEM) were carried out on a Tecnai G2 (F30, FEI) transmission electron microscope operating at 300 kV. The energy-dispersive X-ray (EDX) spectrum was detected on the TEM to analyze the elemental composition. The X-ray diffraction (XRD) patterns were collected by using an X-ray diffractometer (D2 phaser, Bruker) with Cu Kα radiation (λ = 1.54056 Å). A Fluorolog-3 spectrofluorometer (Horiba Jobin Yvon) equipped with a 450 W xenon lamp was used to record the photoluminescence (PL) spectra. The absolute photoluminescence quantum yield (PLQY) was measured on the Edinburgh FLS920 fluorescence spectrometer with a barium-sulfate-coated integrating sphere. An Edinburgh FLS-920T fluorescence spectrophotometer with an nF900 ns flashlamp was used to measure the luminescence decay curves. The X-ray photoelectron spectra (XPS) were collected on a Kratos AXIS Ultra DLD X-ray photoelectron spectrometer. The Fourier transform infrared (FT-IR) spectra were recorded with a Nicolet Nexus 670 spectrometer in the range from 4000 to 400 cm^{-1}. Specific surface areas were calculated using the BET (Brunauer–Emmett–Teller) method with N_2 adsorption–desorption isotherms recorded on a Micromeritics TriStar II 3020 specific surface and porosity analyzer.

ASSOCIATED CONTENT

Supporting Information

The Supporting Information is available free of charge at https://pubs.acs.org/doi/10.1021/acsami.1c20804.

Additional SEM and TEM of Ce-MOF synthesized at different conditions, BET results at different synthesis stages, FDTD and light-extraction diagrams, comparison tables of stabilities and LED properties, EL spectra of LEDs at different currents and different working times (PDF)

AUTHOR INFORMATION

Corresponding Author

Yuhua Wang – *Department of Materials Science, School of Physical Science and Technology, National and Local Joint Engineering Laboratory for Optical Conversion Materials and*

https://doi.org/10.1021/acsami.1c20804
ACS Appl. Mater. Interfaces 2022, 14, 3176–3188

Technology of National Development and Reform Commission, Lanzhou University, Lanzhou 730000, China; orcid.org/0000-0001-7047-4760; Email: wyh@lzu.edu.cn

Authors

Jiejun Ren − *Department of Materials Science, School of Physical Science and Technology, National and Local Joint Engineering Laboratory for Optical Conversion Materials and Technology of National Development and Reform Commission, Lanzhou University, Lanzhou 730000, China*

Andries Meijerink − *Department of Materials Science, School of Physical Science and Technology, National and Local Joint Engineering Laboratory for Optical Conversion Materials and Technology of National Development and Reform Commission, Lanzhou University, Lanzhou 730000, China; Condensed Matter and Interfaces, Debye Institute for Nanomaterials Science, Utrecht University, 3508 TA Utrecht, The Netherlands;* orcid.org/0000-0003-3573-9289

Xiaopeng Zhou − *Department of Materials Science, School of Physical Science and Technology, National and Local Joint Engineering Laboratory for Optical Conversion Materials and Technology of National Development and Reform Commission, Lanzhou University, Lanzhou 730000, China*

Jiapeng Wu − *Department of Materials Science, School of Physical Science and Technology, National and Local Joint Engineering Laboratory for Optical Conversion Materials and Technology of National Development and Reform Commission, Lanzhou University, Lanzhou 730000, China*

Gangyi Zhang − *Department of Materials Science, School of Physical Science and Technology, National and Local Joint Engineering Laboratory for Optical Conversion Materials and Technology of National Development and Reform Commission, Lanzhou University, Lanzhou 730000, China*

Complete contact information is available at: https://pubs.acs.org/10.1021/acsami.1c20804

Author Contributions

All authors have given approval to the final version of the manuscript.

Notes

The authors declare no competing financial interest.

■ ACKNOWLEDGMENTS

The authors gratefully acknowledge the financial support from the National Natural Science Foundation of China (No. U1905213). The authors appreciate Manxin Wang and Nan Zhang for polishing the paper.

■ REFERENCES

(1) Protesescu, L.; Yakunin, S.; Bodnarchuk, M. I.; Krieg, F.; Caputo, R.; Hendon, C. H.; Yang, R. X.; Walsh, A.; Kovalenko, M. V. Nanocrystals of Cesium Lead Halide Perovskites (CsPbX(3), X = Cl, Br, and I): Novel Optoelectronic Materials Showing Bright Emission with Wide Color Gamut. *Nano Lett.* **2015**, *15* (6), 3692−6.

(2) Duan, Y.; Ezquerro, C.; Serrano, E.; Lalinde, E.; García-Martínez, J.; Berenguer, J. R.; Costa, R. D. Meeting High Stability and Efficiency in Hybrid Light-Emitting Diodes Based on SiO2/ZrO2 Coated CsPbBr3 Perovskite Nanocrystals. *Adv. Funct. Mater.* **2020**, *30* (40), 2005401.

(3) Ren, J.; Zhou, X.; Wang, Y. Water triggered interfacial synthesis of highly luminescent CsPbX3:Mn2+ quantum dots from non-luminescent quantum dots. *Nano Research* **2020**, *13* (12), 3387−3395.

(4) Yang, W.; Gao, F.; Qiu, Y.; Liu, W.; Xu, H.; Yang, L.; Liu, Y. CsPbBr3 -Quantum-Dots/Polystyrene@Silica Hybrid Microsphere Structures with Significantly Improved Stability for White LEDs. *Advanced Optical Materials* **2019**, *7* (13), 1900546.

(5) Ren, J.; Dong, X.; Zhang, G.; Li, T.; Wang, Y. Air-stable and water-resistant all-inorganic perovskite quantum dot films for white-light-emitting applications. *New J. Chem.* **2017**, *41* (22), 13961−13967.

(6) Sun, C.; Zhang, Y.; Ruan, C.; Yin, C.; Wang, X.; Wang, Y.; Yu, W. W. Efficient and Stable White LEDs with Silica-Coated Inorganic Perovskite Quantum Dots. *Adv. Mater.* **2016**, *28* (45), 10088−10094.

(7) Lu, X.; Hu, Y.; Guo, J.; Wang, C. F.; Chen, S. Fiber-Spinning-Chemistry Method toward In Situ Generation of Highly Stable Halide Perovskite Nanocrystals. *Adv. Sci. (Weinh)* **2019**, *6* (22), 1901694.

(8) Su, M.; Fan, B.; Li, H.; Wang, K.; Luo, Z. Hydroxyl terminated mesoporous silica-assisted dispersion of ligand-free CsPbBr3/Cs4PbBr6 nanocrystals in polymer for stable white LED. *Nanoscale* **2019**, *11* (3), 1335−1342.

(9) Chiba, T.; Kido, J. Lead halide perovskite quantum dots for light-emitting devices. *Journal of Materials Chemistry C* **2018**, *6* (44), 11868−11877.

(10) Liu, Y.; Li, F.; Qiu, L.; Yang, K.; Li, Q.; Zheng, X.; Hu, H.; Guo, T.; Wu, C.; Kim, T. W. Fluorescent Microarrays of in Situ Crystallized Perovskite Nanocomposites Fabricated for Patterned Applications by Using Inkjet Printing. *ACS Nano* **2019**, *13* (2), 2042−2049.

(11) Chen, D.; Fang, G.; Chen, X. Silica-Coated Mn-Doped CsPb(Cl/Br)3 Inorganic Perovskite Quantum Dots: Exciton-to-Mn Energy Transfer and Blue-Excitable Solid-State Lighting. *ACS Appl. Mater. Interfaces* **2017**, *9* (46), 40477−40487.

(12) He, M.; Cheng, Y.; Shen, L.; Shen, C.; Zhang, H.; Xiang, W.; Liang, X. Mn-doped CsPbCl3 perovskite quantum dots (PQDs) incorporated into silica/alumina particles used for WLEDs. *Appl. Surf. Sci.* **2018**, *448*, 400−406.

(13) Li, J.; Tang, Y.; Li, Z.; Ding, X.; Yu, B.; Lin, L. Largely Enhancing Luminous Efficacy, Color-Conversion Efficiency, and Stability for Quantum-Dot White LEDs Using the Two-Dimensional Hexagonal Pore Structure of SBA-15 Mesoporous Particles. *ACS Appl. Mater. Interfaces* **2019**, *11* (20), 18808−18816.

(14) Yang, D.; Cao, M.; Zhong, Q.; Li, P.; Zhang, X.; Zhang, Q. All-inorganic cesium lead halide perovskite nanocrystals: synthesis, surface engineering and applications. *Journal of Materials Chemistry C* **2019**, *7* (4), 757−789.

(15) Zhang, Q.; Zheng, W.; Wan, Q.; Liu, M.; Feng, X.; Kong, L.; Li, L. Confined Synthesis of Stable and Uniform CsPbBr3 Nanocrystals with High Quantum Yield up to 90% by High Temperature Solid-State Reaction. *Advanced Optical Materials* **2021**, *9* (11), 2002130.

(16) Lee, J.; Min, K.; Park, Y.; Cho, K. S.; Jeon, H. Photonic Crystal Phosphors Integrated on a Blue LED Chip for Efficient White Light Generation. *Adv. Mater.* **2018**, *30* (3), 1703506.

(17) Li, J. S.; Tang, Y.; Li, Z. T.; Li, J. X.; Ding, X. R.; Yu, B. H.; Yu, S. D.; Ou, J. Z.; Kuo, H. C. Toward 200 Lumens per Watt of Quantum-Dot White-Light-Emitting Diodes by Reducing Reabsorption Loss. *ACS Nano* **2021**, *15* (1), 550−562.

(18) Wei, Y.; Cheng, Z.; Lin, J. An overview on enhancing the stability of lead halide perovskite quantum dots and their applications in phosphor-converted LEDs. *Chem. Soc. Rev.* **2019**, *48* (1), 310−350.

(19) Lv, W.; Li, L.; Xu, M.; Hong, J.; Tang, X.; Xu, L.; Wu, Y.; Zhu, R.; Chen, R.; Huang, W. Improving the Stability of Metal Halide Perovskite Quantum Dots by Encapsulation. *Adv. Mater.* **2019**, *31* (28), 1900682.

(20) Krieg, F.; Ochsenbein, S. T.; Yakunin, S.; Ten Brinck, S.; Aellen, P.; Suess, A.; Clerc, B.; Guggisberg, D.; Nazarenko, O.; Shynkarenko, Y.; Kumar, S.; Shih, C. J.; Infante, I.; Kovalenko, M. V. Colloidal CsPbX3 (X = Cl, Br, I) Nanocrystals 2.0: Zwitterionic Capping Ligands for Improved Durability and Stability. *ACS Energy Lett.* **2018**, *3* (3), 641−646.

(21) Pan, J.; Quan, L. N.; Zhao, Y.; Peng, W.; Murali, B.; Sarmah, S. P.; Yuan, M.; Sinatra, L.; Alyami, N. M.; Liu, J.; Yassitepe, E.; Yang, Z.; Voznyy, O.; Comin, R.; Hedhili, M. N.; Mohammed, O. F.; Lu, Z.

H.; Kim, D. H.; Sargent, E. H.; Bakr, O. M. Highly Efficient Perovskite-Quantum-Dot Light-Emitting Diodes by Surface Engineering. *Adv. Mater.* **2016**, *28* (39), 8718−8725.
(22) Hao, J.; Qu, X.; Qiu, L.; Li, G.; Wei, Y.; Xing, G.; Wang, H.; Yan, C.; Jang, H. S.; Cheng, Z.; Lin, J. One-Step Loading on Natural Mineral Halloysite Nanotube: An Effective Way to Enhance the Stability of Perovskite CsPbX3 (X = Cl, Br, I) Quantum Dots. *Advanced Optical Materials* **2018**, *7* (4), 1801323.
(23) Huang, S.; Li, Z.; Kong, L.; Zhu, N.; Shan, A.; Li, L. Enhancing the Stability of CH3NH3PbBr3 Quantum Dots by Embedding in Silica Spheres Derived from Tetramethyl Orthosilicate in "Waterless" Toluene. *J. Am. Chem. Soc.* **2016**, *138* (18), 5749−52.
(24) Jo, J. H.; Heo, H. S.; Lee, K. Assessing Stability of Nanocomposites Containing Quantum Dot/Silica Hybrid Particles with Different Morphologies at High Temperature and Humidity. *Chem. Mater.* **2020**, *32* (24), 10538−10544.
(25) Li, Z.; Kong, L.; Huang, S.; Li, L. Highly Luminescent and Ultrastable CsPbBr3 Perovskite Quantum Dots Incorporated into a Silica/Alumina Monolith. *Angew. Chem., Int. Ed. Engl.* **2017**, *56* (28), 8134−8138.
(26) Liang, P.; Zhang, P.; Pan, A.; Yan, K.; Zhu, Y.; Yang, M.; He, L. Unusual Stability and Temperature-Dependent Properties of Highly Emissive CsPbBr3 Perovskite Nanocrystals Obtained from in Situ Crystallization in Poly(vinylidene difluoride). *ACS Appl. Mater. Interfaces* **2019**, *11* (25), 22786−22793.
(27) Wei, Y.; Deng, X.; Xie, Z.; Cai, X.; Liang, S.; Ma, P. a.; Hou, Z.; Cheng, Z.; Lin, J. Enhancing the Stability of Perovskite Quantum Dots by Encapsulation in Crosslinked Polystyrene Beads via a Swelling-Shrinking Strategy toward Superior Water Resistance. *Adv. Funct. Mater.* **2017**, *27* (39), 1703535.
(28) Wei, Y.; Li, K.; Cheng, Z.; Liu, M.; Xiao, H.; Dang, P.; Liang, S.; Wu, Z.; Lian, H.; Lin, J. Epitaxial Growth of CsPbX3 (X = Cl, Br, I) Perovskite Quantum Dots via Surface Chemical Conversion of Cs2 GeF6 Double Perovskites: A Novel Strategy for the Formation of Leadless Hybrid Perovskite Phosphors with Enhanced Stability. *Adv. Mater.* **2019**, *31* (16), 1807592.
(29) Yoon, H. C.; Lee, S.; Song, J. K.; Yang, H.; Do, Y. R. Efficient and Stable CsPbBr3 Quantum-Dot Powders Passivated and Encapsulated with a Mixed Silicon Nitride and Silicon Oxide Inorganic Polymer Matrix. *ACS Appl. Mater. Interfaces* **2018**, *10* (14), 11756−11767.
(30) Yuan, S.; Chen, D.; Li, X.; Zhong, J.; Xu, X. In Situ Crystallization Synthesis of CsPbBr3 Perovskite Quantum Dot-Embedded Glasses with Improved Stability for Solid-State Lighting and Random Upconverted Lasing. *ACS Appl. Mater. Interfaces* **2018**, *10* (22), 18918−18926.
(31) Wang, S.; Bi, C.; Yuan, J.; Zhang, L.; Tian, J. Original Core−Shell Structure of Cubic CsPbBr3@Amorphous CsPbBrx Perovskite Quantum Dots with a High Blue Photoluminescence Quantum Yield of over 80%. *ACS Energy Letters* **2018**, *3* (1), 245−251.
(32) Cai, Y.; Li, Y.; Wang, L.; Xie, R. J. A Facile Synthesis of Water-Resistant CsPbBr3 Perovskite Quantum Dots Loaded Poly(methyl methacrylate) Composite Microspheres Based on In Situ Polymerization. *Advanced Optical Materials* **2019**, *7* (22), 1901075.
(33) Liu, Z.; Zhang, Y.; Fan, Y.; Chen, Z.; Tang, Z.; Zhao, J.; Lv, Y.; Lin, J.; Guo, X.; Zhang, J.; Liu, X. Toward Highly Luminescent and Stabilized Silica-Coated Perovskite Quantum Dots through Simply Mixing and Stirring under Room Temperature in Air. *ACS Appl. Mater. Interfaces* **2018**, *10* (15), 13053−13061.
(34) Ding, N.; Zhou, D.; Sun, X.; Xu, W.; Xu, H.; Pan, G.; Li, D.; Zhang, S.; Dong, B.; Song, H. Highly stable and water-soluble monodisperse CsPbX3/SiO2 nanocomposites for white-LED and cells imaging. *Nanotechnology* **2018**, *29* (34), 345703.
(35) Chen, Y.; Yu, M.; Ye, S.; Song, J.; Qu, J. All-inorganic CsPbBr3 perovskite quantum dots embedded in dual-mesoporous silica with moisture resistance for two-photon-pumped plasmonic nanoLasers. *Nanoscale* **2018**, *10* (14), 6704−6711.
(36) Dirin, D. N.; Protesescu, L.; Trummer, D.; Kochetygov, I. V.; Yakunin, S.; Krumeich, F.; Stadie, N. P.; Kovalenko, M. V. Harnessing Defect-Tolerance at the Nanoscale: Highly Luminescent Lead Halide Perovskite Nanocrystals in Mesoporous Silica Matrixes. *Nano Lett.* **2016**, *16* (9), 5866−74.
(37) Wang, B.; Zhang, C.; Zheng, W.; Zhang, Q.; Bao, Z.; Kong, L.; Li, L. Large-Scale Synthesis of Highly Luminescent Perovskite Nanocrystals by Template-Assisted Solid-State Reaction at 800 °C. *Chem. Mater.* **2020**, *32* (1), 308−314.
(38) Loiudice, A.; Saris, S.; Oveisi, E.; Alexander, D. T. L.; Buonsanti, R. CsPbBr3 QD/AlOx Inorganic Nanocomposites with Exceptional Stability in Water, Light, and Heat. *Angew. Chem., Int. Ed. Engl.* **2017**, *56* (36), 10696−10701.
(39) Li, Z.-J.; Hofman, E.; Li, J.; Davis, A. H.; Tung, C.-H.; Wu, L.-Z.; Zheng, W. Photoelectrochemically Active and Environmentally Stable CsPbBr3/TiO2Core/Shell Nanocrystals. *Adv. Funct. Mater.* **2018**, *28* (1), 1704288.
(40) Wei, Y.; Xiao, H.; Xie, Z.; Liang, S.; Liang, S.; Cai, X.; Huang, S.; Al Kheraif, A. A.; Jang, H. S.; Cheng, Z.; Lin, J. Highly Luminescent Lead Halide Perovskite Quantum Dots in Hierarchical CaF2Matrices with Enhanced Stability as Phosphors for White Light-Emitting Diodes. *Advanced Optical Materials* **2018**, *6* (11), 1701343.
(41) Sun, J.-Y.; Rabouw, F. T.; Yang, X.-F.; Huang, X.-Y.; Jing, X.-P.; Ye, S.; Zhang, Q.-Y. Facile Two-Step Synthesis of All-Inorganic Perovskite CsPbX3 (X = Cl, Br, and I) Zeolite-Y Composite Phosphors for Potential Backlight Display Application. *Adv. Funct. Mater.* **2017**, *27* (45), 1704371.
(42) Ye, S.; Sun, J. Y.; Han, Y. H.; Zhou, Y. Y.; Zhang, Q. Y. Confining Mn(2+)-Doped Lead Halide Perovskite in Zeolite-Y as Ultrastable Orange-Red Phosphor Composites for White Light-Emitting Diodes. *ACS Appl. Mater. Interfaces* **2018**, *10* (29), 24656−24664.
(43) Hou, J.; Wang, Z.; Chen, P.; Chen, V.; Cheetham, A. K.; Wang, L. Intermarriage of Halide Perovskites and Metal-Organic Framework Crystals. *Angew. Chem., Int. Ed. Engl.* **2020**, *59* (44), 19434−19449.
(44) Yadav, S. K.; Grandhi, G. K.; Dubal, D. P.; de Mello, J. C.; Otyepka, M.; Zboril, R.; Fischer, R. A.; Jayaramulu, K. Metal Halide Perovskite@Metal-Organic Framework Hybrids: Synthesis, Design, Properties, and Applications. *Small* **2020**, *16* (47), 2004891.
(45) Ren, J.; Zhou, X.; Wang, Y. Dual-emitting CsPbX3@ZJU-28 (X = Cl, Br, I) composites with enhanced stability and unique optical properties for multifunctional applications. *Chemical Engineering Journal* **2020**, *391*, 123622.
(46) Zhang, C.; Li, W.; Li, L. Metal Halide Perovskite Nanocrystals in Metal-Organic Framework Host: Not Merely Enhanced Stability. *Angew. Chem., Int. Ed. Engl.* **2021**, *60* (14), 7488−7501.
(47) Cha, J. H.; Noh, K.; Yin, W.; Lee, Y.; Park, Y.; Ahn, T. K.; Mayoral, A.; Kim, J.; Jung, D. Y.; Terasaki, O. Formation and Encapsulation of All-Inorganic Lead Halide Perovskites at Room Temperature in Metal-Organic Frameworks. *J. Phys. Chem. Lett.* **2019**, *10* (9), 2270−2277.
(48) Zhang, D.; Xu, Y.; Liu, Q.; Xia, Z. Encapsulation of CH3NH3PbBr3 Perovskite Quantum Dots in MOF-5 Microcrystals as a Stable Platform for Temperature and Aqueous Heavy Metal Ion Detection. *Inorg. Chem.* **2018**, *57* (8), 4613−4619.
(49) Zhang, D.; Zhou, W.; Liu, Q.; Xia, Z. CH3NH3PbBr3 Perovskite Nanocrystals Encapsulated in Lanthanide Metal-Organic Frameworks as a Photoluminescence Converter for Anti-Counterfeiting. *ACS Appl. Mater. Interfaces* **2018**, *10* (33), 27875−27884.
(50) Zhang, D.; Zhao, J.; Liu, Q.; Xia, Z. Synthesis and Luminescence Properties of CsPbX3@Uio-67 Composites toward Stable Photoluminescence Convertors. *Inorg. Chem.* **2019**, *58* (2), 1690−1696.
(51) Wu, T.; Liu, X.; Liu, Y.; Cheng, M.; Liu, Z.; Zeng, G.; Shao, B.; Liang, Q.; Zhang, W.; He, Q.; Zhang, W. Application of QD-MOF composites for photocatalysis: Energy production and environmental remediation. *Coord. Chem. Rev.* **2020**, *403*, 213097.
(52) Zhang, S.; Xia, W.; Yang, Q.; Valentino Kaneti, Y.; Xu, X.; Alshehri, S. M.; Ahamad, T.; Hossain, M. S. A.; Na, J.; Tang, J.; Yamauchi, Y. Core-shell motif construction: Highly graphitic nitrogen-doped porous carbon electrocatalysts using MOF-derived

https://doi.org/10.1021/acsami.1c20804
ACS Appl. Mater. Interfaces 2022, 14, 3176−3188

carbon@COF heterostructures as sacrificial templates. *Chemical Engineering Journal* **2020**, *396*, 125154.
(53) Zhang, H.-W.; Zhu, Q.-Q.; Yuan, R.; He, H. Crystal engineering of MOF@COF core-shell composites for ultra-sensitively electrochemical detection. *Sens. Actuators, B* **2021**, *329*, 129144.
(54) Yin, Y.; Wang, J.; Li, T.; Hill, J. P.; Rowan, A.; Sugahara, Y.; Yamauchi, Y. Nanoarchitecturing Carbon Nanodot Arrays on Zeolitic Imidazolate Framework-Derived Cobalt-Nitrogen-Doped Carbon Nanoflakes toward Oxygen Reduction Electrocatalysts. *ACS Nano* **2021**, *15* (8), 13240−13248.
(55) Zhang, S.; Yang, Q.; Xu, X.; Liu, X.; Li, Q.; Guo, J.; Torad, N. L.; Alshehri, S. M.; Ahamad, T.; Hossain, M. S. A.; Kaneti, Y. V.; Yamauchi, Y. Assembling well-arranged covalent organic frameworks on MOF-derived graphitic carbon for remarkable formaldehyde sensing. *Nanoscale* **2020**, *12* (29), 15611−15619.
(56) Meng, L.; Zhang, L.; Zhu, Y.; Jiang, H.; Kaneti, Y. V.; Na, J.; Yamauchi, Y.; Golberg, D.; Jiang, H.; Li, C. Highly dispersed secondary building unit-stabilized binary metal center on a hierarchical porous carbon matrix for enhanced oxygen evolution reaction. *Nanoscale* **2021**, *13* (2), 1213−1219.
(57) Zhang, C.; Wang, B.; Li, W.; Huang, S.; Kong, L.; Li, Z.; Li, L. Conversion of invisible metal-organic frameworks to luminescent perovskite nanocrystals for confidential information encryption and decryption. *Nat. Commun.* **2017**, *8* (1), 1138.
(58) Ren, J.; Li, T.; Zhou, X.; Dong, X.; Shorokhov, A. V.; Semenov, M. B.; Krevchik, V. D.; Wang, Y. Encapsulating all-inorganic perovskite quantum dots into mesoporous metal organic frameworks with significantly enhanced stability for optoelectronic applications. *Chemical Engineering Journal* **2019**, *358*, 30−39.
(59) Shen, J.; Wang, Y.; Zhu, Y.; Gong, Y.; Li, C. A polymer-coated template-confinement CsPbBr3 perovskite quantum dot composite. *Nanoscale* **2021**, *13* (13), 6586−6591.
(60) Li, K.; Yang, J.; Huang, R.; Lin, S.; Gu, J. Ordered Large-Pore MesoMOFs Based on Synergistic Effects of TriBlock Polymer and Hofmeister Ion. *Angew. Chem., Int. Ed. Engl.* **2020**, *59* (33), 14124−14128.
(61) Ahmed, T.; Seth, S.; Samanta, A. Boosting the Photoluminescence of CsPbX3 (X = Cl, Br, I) Perovskite Nanocrystals Covering a Wide Wavelength Range by Postsynthetic Treatment with Tetrafluoroborate Salts. *Chem. Mater.* **2018**, *30* (11), 3633−3637.
(62) Qiu, L. G.; Xu, T.; Li, Z. Q.; Wang, W.; Wu, Y.; Jiang, X.; Tian, X. Y.; Zhang, L. D. Hierarchically micro- and mesoporous metal-organic frameworks with tunable porosity. *Angew. Chem., Int. Ed. Engl.* **2008**, *47* (49), 9487−91.
(63) Li, Z.-T.; Li, J.-X.; Li, J.-S.; Deng, Z.-H.; Deng, Y.-H.; Tang, Y. Scattering Effect on Optical Performance of Quantum Dot White Light-Emitting Diodes Incorporating SiO_2 Nanoparticles. *IEEE J. Quantum Electron.* **2020**, *56* (3), 1−9.
(64) Haque, A.; Ravi, V. K.; Shanker, G. S.; Sarkar, I.; Nag, A.; Santra, P. K. Internal Heterostructure of Anion-Exchanged Cesium Lead Halide Nanocubes. *J. Phys. Chem. C* **2018**, *122* (25), 13399−13406.
(65) MacAdam, D. L. Visual sensitivities to color differences in daylight. *J. Opt. Soc. Am.* **1942**, *32* (5), 247−274.

https://doi.org/10.1021/acsami.1c20804
ACS Appl. Mater. Interfaces 2022, 14, 3176−3188